Axial magnetic anomalies over slow-spreading ridge segments: insights from numerical 3-D thermal and physical modelling

Sébastien Gac, Jérôme Dyment, Chantal Tisseau, Jean Goslin

Geophys. J. Int. (2003) **154,** 618–632

Axial magnetic anomalies over slow-spreading ridge segments: insights from numerical 3-D thermal and physical modelling

Sébastien Gac, Jérôme Dyment,* Chantal Tisseau and Jean Goslin

CNRS UMR 6538 *Domaines Océaniques, Institut Universitaire Européen de la Mer, Université de Bretagne Occidentale, Brest, France.*
E-mails: sgac@sdt.univ-brest.fr; jdy@ipgp.jussieu.fr; tisseau@univ-brest.fr; goslin@univ-brest.fr

Accepted 2003 February 25. Received 2003 February 25; in original form 2002 January 28

SUMMARY

The axial magnetic anomaly amplitude along Mid-Atlantic Ridge segments is systematically twice as high at segment ends compared with segment centres. Various processes have been proposed to account for such observations, either directly or indirectly related to the thermal structure of the segments: (1) shallower Curie isotherm at segment centres, (2) higher Fe-Ti content at segment ends, (3) serpentinized peridotites at segment ends or (4) a combination of these processes. In this paper the contribution of each of these processes to the axial magnetic anomaly amplitude is quantitatively evaluated by achieving a 3-D numerical modelling of the magnetization distribution and a magnetic anomaly over a medium-sized, 50 km long segment. The magnetization distribution depends on the thermal structure and thermal evolution of the lithosphere. The thermal structure is calculated considering the presence of a permanent hot zone beneath the segment centre. The 'best-fitting' thermal structure is determined by adjusting the parameters (shape, size, depth, etc.) of this hot zone, to fit the modelled geophysical outputs (Mantle Bouguer anomaly, maximum earthquake depths and crustal thickness) to the observations. Both the thermoremanent magnetization, acquired during the thermal evolution, and the induced magnetization, which depends on the present thermal structure, are modelled. The resulting magnetic anomalies are then computed and compared with the observed ones. This modelling exercise suggests that, in the case of aligned and slightly offset segments, a combination of higher Fe-Ti content and the presence of serpentinized peridotites at segment ends will produce the observed higher axial magnetic anomaly amplitudes over the segment ends. In the case of greater offsets, the presence of serpentinized peridotites at segment ends is sufficient to account for the observations.

Key words: magnetic anomalies, magnetization, mid-ocean ridges, numerical techniques, thermal structure.

1 INTRODUCTION

Bathymetric studies conducted along slow-spreading mid-ocean ridges have revealed the existence of a short (typically less than 100 km) wavelength segmentation (Le Douaran & Francheteau 1981; Macdonald *et al.* 1984, 1986). Along the Mid-Atlantic Ridge (MAR) segment lengths range between 15 and 90 km (Sempéré *et al.* 1990, 1993).

Geophysical observations along MAR segments provide information on the thermal structure of slow-spreading ridge segments. Gravity studies carried out over various portions of the MAR (Kuo & Forsyth 1988; Lin *et al.* 1990; Detrick *et al.* 1995; Thibaud *et al.* 1998) show an increase of the Mantle Bouguer Anomaly (MBA, which reflects variations in the crustal thickness and/or the mantle and/or crustal densities) from segment centres to segment ends. These variations are attributed to crustal thickening at segment centres (Kuo & Forsyth 1988; Lin *et al.* 1990), which in turn suggests focused magma production beneath segment centres. Another contribution to the MBA would come from the presence of a lower density mantle and crust under the segment centres, which reflects higher temperatures at segment centres relative to segment ends. The density structure constrained by the MBA is therefore consistent with the upwelling of hot material beneath segment centres (Lin *et al.* 1990). The MBA alone does not allow one to quantify both the crustal thickness variation and the density structure, essentially because the inversion of the MBA in terms of crustal thickness variation is underconstrained. Other observations are therefore necessary to better constrain the thermal structure of slow-spreading centres.

Microseismicity studies show that the maximum depth of earthquakes increases from segment centres to segment ends (Kong *et al.*

*Now at: CNRS UMR 7097 Laboratoire de Géosciences Marines, Institut de Physique du Globe, Paris, France.

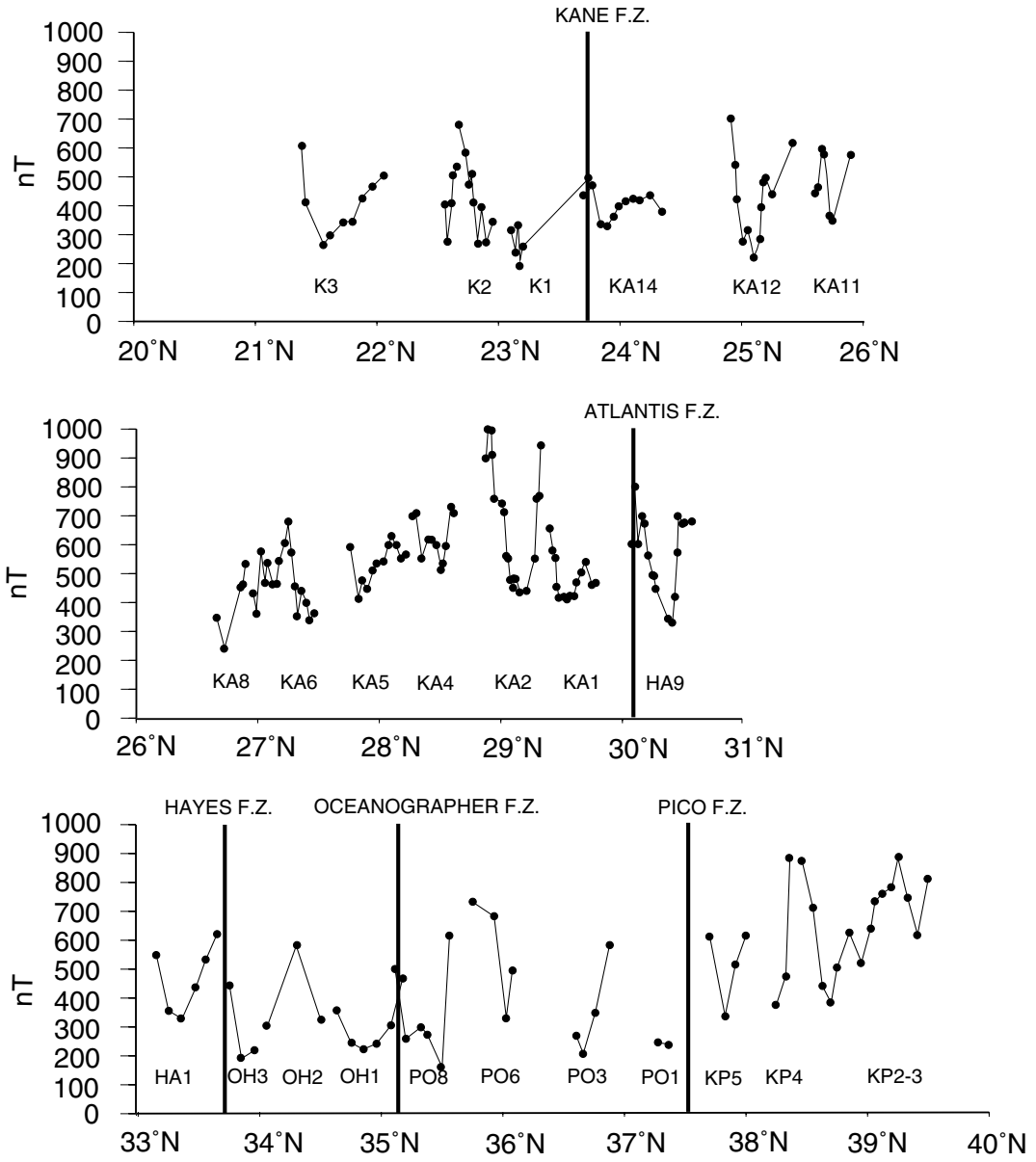

Figure 1. Amplitude of the axial magnetic anomaly, observed over segments of the Mid-Atlantic Ridge between 20°N and 40°N (from Ravilly *et al.* 1998). Segments are indexed according to the nomenclature proposed by Detrick *et al.* (1995). Solid circles indicate the amplitudes measured along surface across-axis magnetic anomaly profiles. Thick vertical lines indicate major fracture zones.

1992; Barclay *et al.* 1993; Toomey *et al.* 1993; Wolfe *et al.* 1995), thus reflecting a deepening of the brittle–ductile transition, i.e. of the 800 °C isotherm, towards the segment ends (Kong *et al.* 1992). Seismic refraction experiments (Tolstoy *et al.* 1993; Canales *et al.* 2000; Hooft *et al.* 2000) show that the crust progressively thins from segment centres to segment ends, an observation consistent with the frequent outcropping of mantle rocks at segment ends (Juteau *et al.* 1990; Cannat 1993; Cannat *et al.* 1995). These observations also support the hypothesis of upwelling hot material beneath the segment centres and provide constraints on the 3-D thermal structure of the segments. However, such observations are only available on a limited number of segments.

On the other hand, observations of the axial magnetic anomaly signal are available on many segments. For example, Ravilly *et al.* (1998) compiled magnetic profiles across the MAR axis between 20° and 40°N (Fig. 1) and studied the variation of axial magnetic anomaly amplitude over 20 ridge segments. These authors have shown that this amplitude is systematically twice as high as at segment ends compared with segment centres.

Various processes have been proposed to account for such an along-axis variation of the axial magnetic anomaly amplitude:

(1) more intense fracturing and hydrothermal circulation at the segment centres, yielding lower basalt magnetization as a result of pervasive alteration of titanomagnetite to titanomaghemite (Rona 1978; Wooldridge *et al.* 1992);

(2) a thinner magnetized layer due to a shallower Curie isotherm at the segment centres (Grindlay *et al.* 1992);

(3) higher Fe-Ti content at segment ends yielding higher basalt magnetization (Weiland *et al.* 1996). Such Fe-Ti content variation

would be due to the variation in the degree of fractionation, resulting from a decrease of temperature from the segment centres to ends;

(4) serpentinized peridotites at segment ends (Pockalny *et al.* 1995; Pariso *et al.* 1996). In the presence of seawater and at relatively low temperatures, peridotite is altered to serpentinite, with the creation of magnetite. To produce high magnetic anomaly amplitudes, the temperature at segment ends should be low enough to allow for a significant amount of serpentinized peridotites.

All of these processes, except possibly the first one, are directly or indirectly related to the thermal structure and evolution of the segments, and so would be the axial magnetic anomaly amplitudes. A quantitative evaluation of their relative contributions to the amplitude of the axial magnetic anomaly will therefore provide constraints on the thermal structure of segments. In this paper, we develop a 3-D numerical model of the thermal structure and evolution and of the resulting distributions of densities and magnetizations for a medium-sized (50 km) segment, typical of a slow-spreading ridge. This model is used to discriminate among the various processes proposed to explain the axial magnetic anomaly amplitude for different geometries of a slow-spreading centre.

2 THERMAL SIMULATION OF A SLOW-SPREADING RIDGE SEGMENT

Basic equation and computational methods

Geophysical and petrological observations carried out on slow-spreading ridges clearly favour a 3-D thermal structure, so the computations are performed in a parallelepipedic box. The along-axis length of the box is set to 50 km, which is the average length of MAR segments. To allow the calculation of magnetic anomalies over crust created during the last 10 Myr with a spreading rate of 1 cm yr^{-1}, the across-axis width of the box is set to 200 km. The depth of the box is fixed to 100 km, which corresponds to the average thickness of the lithosphere far from the ridge axis.

As previously proposed from geophysical observations, the thermal structure of a slow-spreading ridge segment requires the presence of a hot zone, located beneath the centre of the segment. Such a hot zone is imposed *a priori* in our models: temperatures are kept constant within the hot zone, simulating the adiabatic upwelling of asthenospheric material. The hot zone is assumed to be permanent, i.e. neither the magmato-tectonic cycles of ~1 Myr (Tisseau & Tonnerre 1995) nor the average lifetime of 3–9 Myr for a segment (Gente *et al.* 1995) are considered here.

The thermal structure resulting from the presence of a hot zone is computed using the heat equation. Heat transfer takes place by conduction in the three directions, by advection due to the horizontal spreading plate motion, and by loss of heat due to melting (Tisseau & Tonnerre 1995). The heat equation can then be written as

$$\frac{\partial T(x,y,z,t)}{\partial t} = K\left(\frac{\partial^2}{\partial x^2}+\frac{\partial^2}{\partial y^2}+\frac{\partial^2}{\partial z^2}\right)T(x,y,z,t) - U_x\frac{\partial T(x,y,z,t)}{\partial x} - \frac{L}{C_p}\frac{\partial \Phi(x,y,z,t)}{\partial t}, \quad (1)$$

where the degree of partial melting Φ is

$$\Phi(x,y,z,t) = \frac{T - T_{\mathrm{sol}}}{L/C_p} \quad (2)$$

with the solidus given by

$$T_{\mathrm{sol}} = 1115 + 12p, \quad (3)$$

where K is the thermal diffusivity ($K = 1.13 \times 10^{-6}$ m^2 s^{-1}), U_x is the spreading rate ($U_x = 1$ cm yr^{-1}), L is the latent heat of partial melting ($L = 600$ kJ kg^{-1}), C_p is the specific heat ($C_p = 1$ kJ kg^{-1} °C^{-1}), T is the temperature in °C and p is the pressure in kbar.

The existence of a hot zone beneath the segment centre induces higher temperatures at segment centres compared with segment ends. Consequently, isotherms (including the Curie isotherm) deepen from segment centres to segment ends. Such a temperature distribution is consistent with an increasing degree of fractionation and higher Fe-Ti content toward segment ends.

It should be stressed that a segment is not thermally insulated and undergoes thermal influence from its neighbours. A realistic calculation of the thermal structure of a segment thus requires to take into account the thermal influence of the adjacent segments. If we consider a segment in line with identical neighbours, there is no thermal transfer between segments: for this reason we impose the null flux (Neumann) condition on the vertical walls of the model box, which are perpendicular to the ridge axis. In the case of offset segments, the thermal structure of two adjacent segments is computed inside the model box. The vertical walls of the model box, perpendicular to the ridge axis, cross the centres of each segment. Null flux conditions are imposed on these boundaries. The computed thermal structure is therefore symmetric relative to those vertical boundaries.

The heat equation is solved numerically in 3-D by a finite-difference method (algorithm developed by Trutin (1995) following Yanenko's method (1968) with fractional steps and Noye's disintegration technique (1984)). The resulting thermal structure is obtained after 1000 iterations (of 10 000 yr each) have been performed, thus reaching a quasi-stationary state.

Determination of the 'best-fitting' thermal structure

Three geophysical outputs (the variation of MBA between segment centres and segment ends, the crustal thickness variation along the segment and the maximum depth of microseismicity at segment centres and segment ends (see below)), which depend on temperature, are modelled from the thermal structure. The thermal structure, and therefore the resulting model outputs, are directly controlled by the shape (geometry and dimensions) of the hot zone. The different model outputs are compared simultaneously with the observations for different geometry and dimensions of the hot zone, until we obtain the geometry and dimensions producing modelled geophysical outputs which fit the observed ones. The corresponding thermal structure is called the 'best-fitting' thermal structure hereafter. The parameters which characterize the hot zone producing this best-fitting thermal structure are referred to as 'best-fitting parameters'.

Thibaud *et al.* (1998) have compiled bathymetric and gravity data along 51 segments of the MAR between 15°and 40°N. They correlate the variation of MBA between segment centres and segment ends (denoted hereafter as ΔMBA) to the segment length, with the longest segments displaying the strongest ΔMBA amplitude. The correlation between ΔMBA amplitude and segment length is linear, with a slope ranging between 0.4 and 0.5 mGal km^{-1} (Detrick *et al.* 1995; Thibaud *et al.* 1998). The average observed value of ΔMBA amplitude for 50 km long segments ranges between 20 and 25 mGal.

Microseismicity data, collected along four segments of the MAR at 23°N (Toomey *et al.* 1985, 1988), 26°N (Kong *et al.* 1992), 29°N (Wolfe *et al.* 1995) and 35°N (Barclay *et al.* 1993), show that the maximum depth of earthquakes increases from the segment centres to segment ends. At segment ends, the earthquake foci reach a

maximum depth of 9 ± 1 km. At segment centres this depth is generally shallower, less than 4 km at 26°N and 35°N and between 2 and 5 km at 29°N. This has been interpreted as reflecting a deepening of the brittle–ductile transition towards segment ends (Kong *et al.* 1992).

The crustal structure of slow-spreading ridge segments has been derived from seismic refraction experiments carried out in the North (Canales *et al.* 2000; Hooft *et al.* 2000) and South Atlantic (Tolstoy *et al.* 1993). These experiments also indicate a thicker crust at segment centres compared with segment ends. For segment OH1 (35°N), which is a 90 km long segment, seismic interpretation indicates a Moho 8.1 km deep beneath the segment centre and 4–5 km deep beneath the segment ends (Canales *et al.* 2000). However, the seismic Moho at segment ends may differ from the crust/mantle petrological limit as the densities of serpentinized peridotites, and thus their seismic velocities, may be comparable to those observed in the gabbros of the lower crust (Horen *et al.* 1996). Consequently, the crustal thickness can decrease by up to 50 per cent or more from a segment centre to a segment end, and may totally vanish, as suggested by the many outcrops of peridotite observed at segment ends (Juteau *et al.* 1990; Cannat 1993; Cannat *et al.* 1995).

The next sections describe how the computed outputs are simulated.

Brittle–ductile boundary

The brittle–ductile boundary is thought to correspond to the 750 °C isotherm for peridotite and to the 500 °C isotherm for the oceanic crust (Chen & Molnar 1983). If the segment centre is hot enough, then the 500 °C isotherm lies within the crust and limits the maximum depth of earthquakes. At segment ends, the maximum depth of the earthquakes corresponds to 750 °C isotherm.

Crustal thickness

Melt is extracted from the partially molten mantle to produce the crust when the degree of partial melting exceeds 3 per cent (McKenzie 1984). Seismic refraction experiments indicate that a non-steady and discontinuous magma chamber exists on the Mid-Atlantic Ridge (Sinton & Detrick 1992; Calvert 1995), suggesting that the along-axis melt migration is very limited beneath slow-spreading ridges compared with fast-spreading ridges, where persistent and continuous along-strike magma chambers have been observed (Lin & Phipps Morgan 1992). These results are supported by geochemical analyses of lava samples dredged along the 26°S segment of the Mid-Atlantic Ridge (Niu & Batiza 1994), which show that the segment would be fed by different parental melt batches. Such an observation seemingly precludes important along-axis melt transport. For these reasons and for simplicity, we assume that liquids extracted within a vertical section perpendicular to the axis produce crust at the ridge axis in the same section and we do not consider possible along-axis liquid transport. Additionally, we estimate that only a fraction of the extracted liquid reaches the surface. This fraction is adjusted to produce a 6 km thick crust (average thickness of the normal oceanic crust) at the centre of each segment. The rate of extraction is constant along the axis: the variation of crustal thickness is proportional to that of the melting zone volume along the segment.

MBA: determination of the densities

The MBA deduced from the gravity observations reflects variations of the crustal thickness and/or variations of crustal and/or mantle densities. We consider density variations from several origins. The thermal structure results in lateral density variations due to thermal expansion and to the presence of liquid in the melting zone. The density variation can be written as

$$\rho = \rho_0(1 - \alpha T - \beta\Phi), \tag{4}$$

where $\alpha = 3 \times 10^{-5}\ ^\circ\mathrm{C}^{-1}$, $\beta = 0.152$ (Scott & Stevenson 1989), T is the temperature in °C and Φ is the degree of partial melting in per cent.

These density variations add to the density contrast between the crust (2800 kg m^{-3} at 0 °C) and the mantle (3300 kg m^{-3} at 0 °C).

Density variations due to serpentinization

The serpentinization of peridotites significantly lowers their density (Christensen 1966). The density depends linearly on the serpentinization rate (Miller & Christensen 1997). Serpentinization is mainly controlled by temperature and the amount of water that is available (Macdonald & Fyfe 1984). In the presence of water, serpentinization occurs for temperatures ranging from 200 to 400 °C (Caruso & Chernosky 1979; Bideau *et al.* 1991; Agrinier *et al.* 1995). Serpentinized peridotites are observed only at segment ends, as isotherms corresponding to the serpentinization front deepen from segment centres to segment ends. The lithosphere is fractured and water can penetrate down to the brittle–ductile transition. However, increasing lithostatic pressure with depth tends to close fissures and water does not circulate as easily in the deep crust as it does at shallower depths, making serpentinization more difficult. The interpretation of seismic profiles recorded over segment ends near 35°N (Canales *et al.* 2000) confirms such an evolution of serpentinization with depth. Serpentinization rates deduced from seismic velocities range from 40 per cent at 4 km to 10 per cent at 6 km below the seafloor. Several studies further suggest that serpentinization takes place mainly at the ridge axis. Heat flow simulations (Becker *et al.* 1989; Fisher *et al.* 1990; Fisher *et al.* 1994) indeed indicate that, off-axis, water does not penetrate within the crust below the first few hundred metres, precluding serpentinization at greater depths. These results agree with seismic studies which show that, further than 15–20 km off-axis, the seismic velocity in the lower crust does not vary significantly (Francis 1981).

We estimate the proportion of serpentinite in the mantle rocks by considering that peridotite is altered to serpentine between 400 °C and 200 °C in the presence of water. The presence of water is taken into account by multiplying the rate of serpentinization by a coefficient equal to 1 at the surface and decreasing exponentially to 0 at the brittle–ductile transition depth.

The 'best-fitting' thermal model

For different parameters of the hot zone, the computed outputs are compared simultaneously with the observed variations of MBA, crustal thickness and maximum depth of microseismicity along slow-spreading ridge segments, until the 'best-fitting' thermal structure is obtained.

The geometry of the mantle upwelling beneath slow-spreading ridges ranges between two end-members: focused upwelling under segment centres (Whitehead *et al.* 1984; Lin *et al.* 1990), or sheet-like along-axis upwelling, dammed by fracture zones (Magde & Sparks 1997; Magde *et al.* 1997). We have considered two geometries reflecting these types of upwelling (Fig. 2). The first geometry (denoted as A) has an elliptic section, is broader at segment

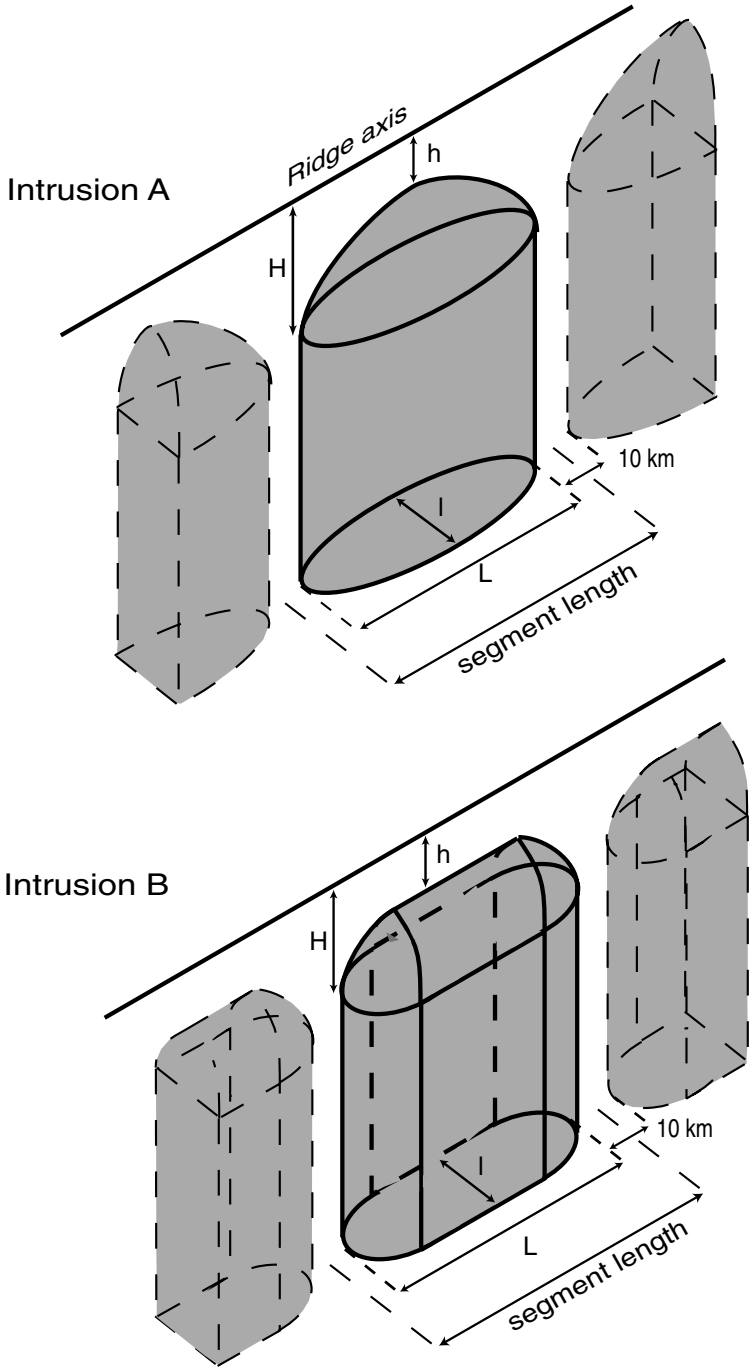

Figure 2. The intrusion geometry is characterised by four parameters: H is the depth to the top of the cylindrical upper part of the intrusion, h is the depth to the top of of the intrusion. L is the length of the intrusion along-axis, and l is the width of the intrusion across axis. Intrusion A (top) simulates a focused upwelling of hot material towards the segment centre, intrusion B simulates a distributed upwelling along the whole segment.

centres and gradually thins towards segment ends, and is topped by a paraboloid. The second geometry (denoted as B) has a constant-width section and a flat top along most of the segment length, in order to simulate a uniform upwelling along the segment. On a section perpendicular to the axis, the top of the hot zone deepens when moving away from the axis. For both geometries we identify four parameters: the depth to the top of the intrusion at the segment centre (h) and at the segment end (H), and the length (L) and width (l) of the base of the intrusion (Fig. 2).

Slow-spreading ridge segments are separated by non-transform discontinuities for which the typical along-axis length is 10 km (Pockalny *et al.* 1988; Tucholke & Schouten 1988; Sempéré *et al.* 1993). In these discontinuities, the magmatic activity is very reduced or even non-existent. To take into account the presence of such

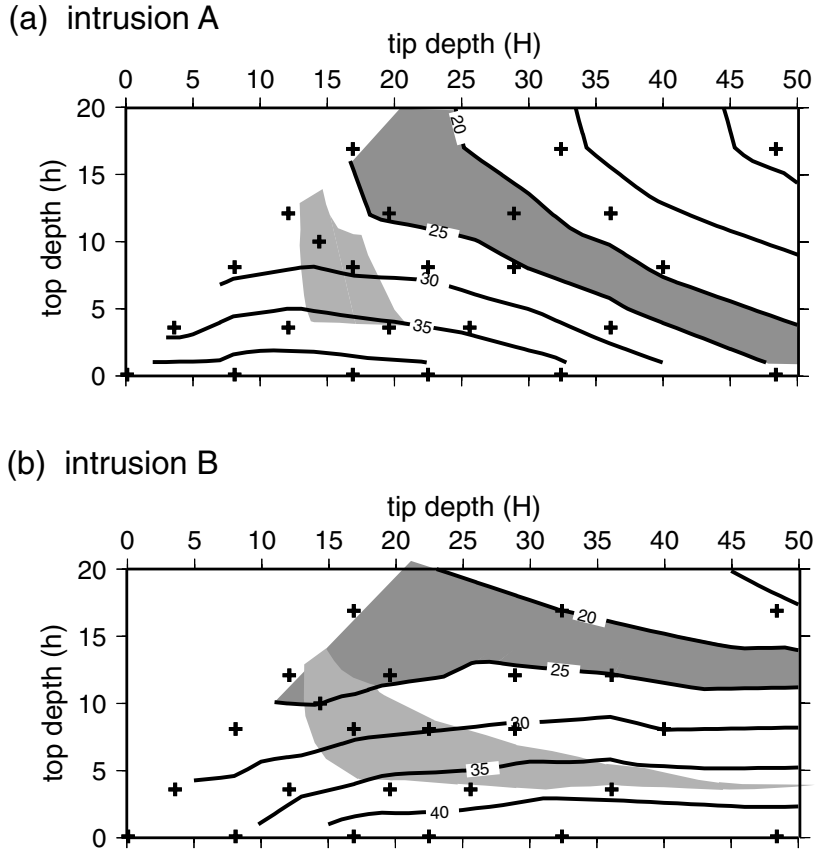

Figure 3. Determination of the 'best-fitting' parameters h and H, in the cases of intrusion shape and B (see caption of Fig. 2 for their definition) Crosses show the couples (h, H) for which the geophysical outputs are calculated. The values of these outputs are interpolated within the range of investigated h and H. Thick lines represent the ΔMBA between segment centres and segment ends. The lighter grey region represents the range of parameters h and H accounting fot the observed maximal depths of the earthquakes. The darker grey region represents the range of parameters h and H accounting for the observed ΔMBA amplitude.

discontinuities, we set a distance of 10 km between two adjacent thermal intrusions. For a 50 km long segment, this results in setting to 40 km the length L of each thermal intrusion (see Fig. 2). Varying the width l of the intrusion from 10 to 40 km results in a change in ΔMBA amplitude smaller than 5 mGal, that is to say largely negligible compared with the variation produced by varying H and h. The width l was therefore set to a constant 20 km, which corresponds to the average width of the diapirs observed in the Oman ophiolites (Nicolas 1989). For the two geometries A and B, observations on the brittle–ductile transition depths are accounted for by allowing h to range from 8 to 12 km (10 km average) and H to range from 13 to 17 km (15 km average). At the segment centre, the models predict average depths of 3–4 km for the 500 °C isotherm and of 8 km for the 750 °C isotherm. For geometry A, there are no values of h and H that succeed in accounting for all geophysical observations (Fig. 3a): any values of h and H within the range 10 ± 2 and 15 ± 2 km result in a too high ΔMBA amplitude (28 mGal), in relation to the large variation of crustal thickness that results from the elliptic section of the hot zone. On the other hand, for geometry B, which depicts a constant-width hot zone along most of the segment length, the crustal thickness variation between the centre and ends is reduced and the value of ΔMBA amplitude is consequently lower, about 23 mGal, a value which fits the observations. Geometry B therefore accounts for all geophysical observations on a 50 km long segment (Fig. 3b) when h is equal to 10 ± 2 km and H to 15 ± 2 km. Fig. 4 shows the thermal structure and simulated geophysical outputs for these 'best-fitting' values of H and h.

It should be noted that at this stage the geometry and dimensions of the intrusion have been determined in the case of aligned segments. Introduction of an offset between adjacent segments would result in cooler segment ends, with deeper isotherms, resulting in lower crustal production at segment ends. Additional tests showed that such offsets generate only minor changes in the values of the modelled geophysical data, lower than the uncertainties on the geophysical observations. Indeed, a more pronounced crustal attenuation as a result of deeper isotherms will increase the thickness of the serpentinized peridotite layer at segment ends. This effect in turn compensates for the larger crustal attenuation at segment ends and generates ΔMBA amplitude values similar to those modelled for segments with no offsets.

3 COMPUTATION OF MAGNETIZATION AND AXIAL MAGNETIC ANOMALY AMPLITUDES

Rocks of the oceanic crust and the uppermost mantle contain magnetic minerals and generally carry a magnetization. The distribution of magnetization depends on the magnetic properties of each type of rock and on the petrological structure of the lithosphere, which,

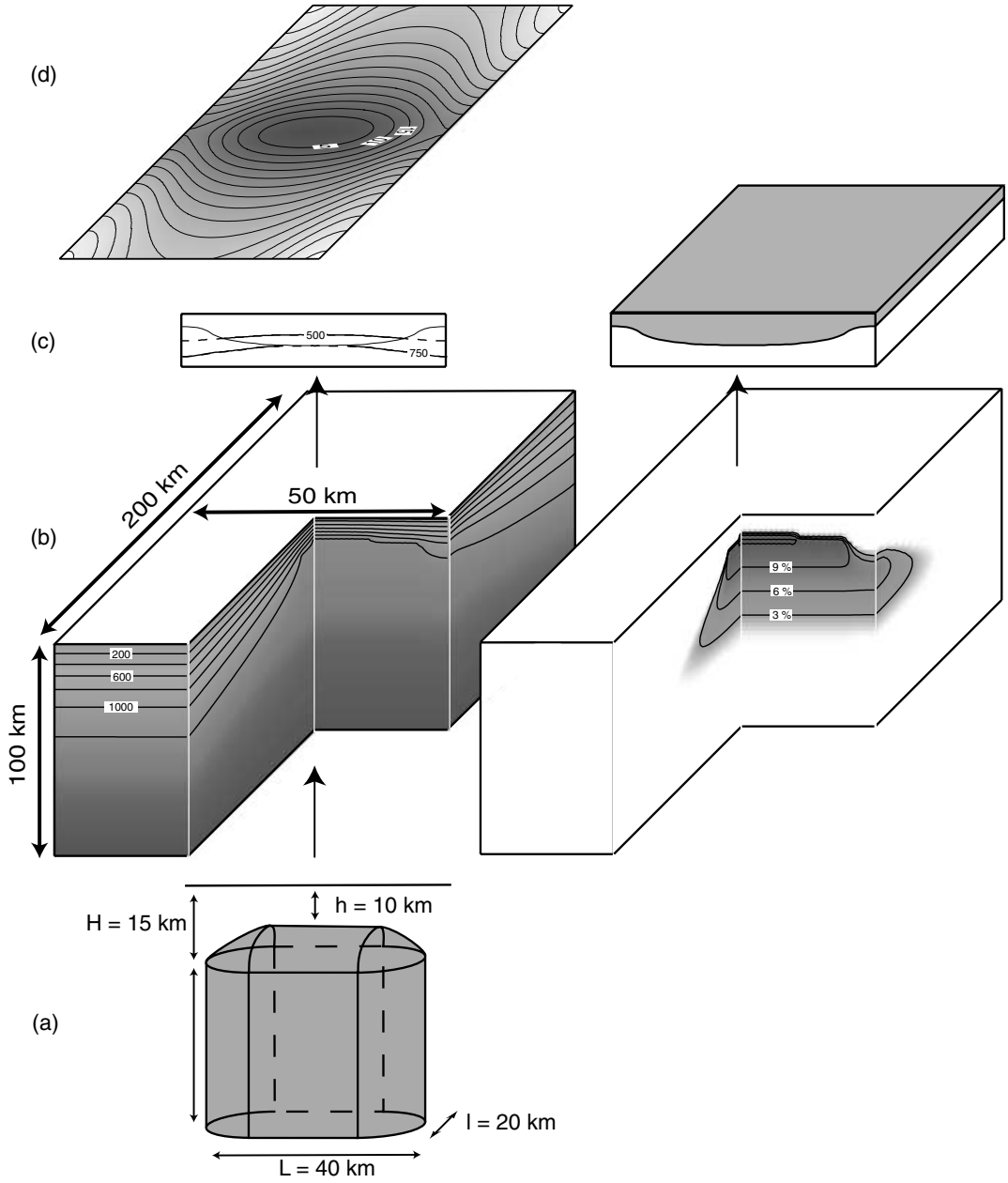

Figure 4. Model outputs. (a) The 'best-fitting' intrusion geometry. (b) Modelled thermal structure (left) and distribution of the partial melting rate (right). (c) Along-axis crustal sections. *Left*: the thin line represents the Moho, the thick lines 500 and 750 °C isotherms, marking the maximal depth of the earthquake in the crust and in the mantle, respectively. At the segment centre the 500 °C isotherm is 4 km below the seafloor. At the segment ends, the 750 °C isotherm is 8 km deep. *Right*: crustal thickness. The crust is 6 km thick at the the segment centre and 2–3 km thick at the ends. (d) Modelled MBA reproducing the circular shape ('bull's eye') observed over the segment centre. From the centre towards the segment ends, the ΔMBA amplitude is 23 mGal.

in turn, results from the thermal structure and the thermal evolution of the lithosphere.

Different types of magnetization

Three types of magnetization are considered.

Thermoremanent magnetization

Thermoremanent magnetization (TRM) is acquired during the cooling of magnetic minerals under their blocking (or Curie) temperatures. The blocking temperatures of titanomagnetite, the dominant magnetic mineral in the extrusive basalts, range between 160 and 420 °C. A magnetic blocking temperature range of 520–580 °C is taken for magnetite, the dominant magnetic mineral in other oceanic rocks (intrusive basalts, gabbros and serpentinized peridotites, Dunlop & Prévot 1982).

While moving away from the axis, a lithospheric column progressively cools beneath the range of blocking Curie temperatures and acquires a thermoremanent magnetization. Rocks at the top of the column cool relatively faster and acquire their magnetization right at the axis, whereas deeper rocks can remain hot for a longer

Table 1. Magnetic properties of the different lithologies considered in this paper.

	Extrusive basalt	Intrusive basalt	Olivine gabbro	Peridotite
Kind of magnetization	TRM	TRM	Serpentinization	Serpentinization
Magnetic mineral	Titanomagnetite	Magnetite	Magnetite	Magnetite
T_{Curie}	160–420 °C	520–580 °C	520–580 °C	520–580 °C
$T_{\text{acquisition}}$ first magnetization	idem	idem	200–400 °C	200–400 °C
Increase factor in magnetization	2–3	2–3		
Maximum magnetization	10 A m^{-1}	0.5 A m^{-1}	0–1 A m^{-1}	0–7 ± 3A m^{-1}
Q (Koenigsberger ratio)	8	8	8	0.5–2

period of time and acquire their magnetization later, further off-axis (Arkani-Hamed 1989).

Chemical remanent magnetization

The magnetite contained in olivine-rich rocks is generally a by-product of low-temperature serpentinization of olivine. As serpentinization occurs for temperatures lower than the Curie temperatures of magnetite, peridotites acquire a chemical remanent magnetization (CRM) as serpentinization progresses, i.e. when the lithosphere cools beneath ∼400 °C while moving away from the axis (assuming the presence of water, see above).

Together with their thermal evolution, the succession of geomagnetic field reversals with time determines the acquisition of a normal or inverse remanent magnetization by the rocks. The distribution of TRM is computed following the algorithm of Arkani-Hamed (1989) and Dyment & Arkani-Hamed (1995). The distribution of CRM is computed following the algorithm of Dyment *et al.* (1997).

Other remanent magnetizations are negligible with respect to the TRM and CRM. Furthermore, we will assume that the higher natural remanent magnetization (NRM) measured on rock samples represents a maximum value of the TRM, or CRM according to the type of rock (i.e. the magnetization that would be acquired after an infinite time under a constant-polarity geomagnetic field).

Induced magnetization

The magnetization induced by the present-day geomagnetic field may have a significant contribution to marine magnetic anomalies as long as the magnetized sources are laterally heterogeneous. The induced magnetization, parallel to the present magnetic field, is written as

$$\text{Ai} = K B = M/Q, \tag{5}$$

where K is the susceptibility of the rock, B is the intensity of the magnetic field, M is the maximum remanent magnetization and Q is the Koenigsberger ratio.

The intensity of induced magnetization also depends on the temperature (e.g. Pozzi & Dubuisson 1992): the magnetic susceptibility increases gradually with temperature, reaches a maximum (about twice its initial value) for temperatures immediately below the Curie temperatures (Hopkinson effect), and abruptly falls to zero at the Curie temperature. The induced magnetization thus becomes

$$\text{Ai} = \chi(T)M/Q \tag{6}$$

with

$$\chi(T) = K(T)/K(T_0), \tag{7}$$

where T is the rock temperature and T_0 the laboratory ambient temperature (∼20 °C).

In eq. (6), only the Koenigsberger ratio depends on the type of rock.

The different types of rock and their magnetic properties

Oceanic crust is built of extrusive basalt, intrusive basalt and gabbro. In this paper we only consider olivine gabbro, as ferrogabbro represents only a small proportion (∼10 per cent) of the lower crust (Pariso & Johnson 1993). In the uppermost mantle, serpentinized peridotite carries a significant magnetization and probably contributes to the magnetic anomalies (Arkani-Hamed 1988; Nazarova 1994; Dyment *et al.* 1997). Table 1 summarizes the magnetic properties of each lithology.

Basalt

A 6 km thick reference crust (at the centre of the segment) comprises a 0.5 km thick layer of extrusive basalt and a 1.5 km thick layer of intrusive basalt. Extrusive and intrusive basalts, for which the main magnetic minerals are, respectively, titanomagnetite and magnetite, acquire a thermoremanent magnetization and carry an induced magnetization.

Natural remanent magnetization (NRM) measurements on young extrusive basalt samples (0–20 Myr) typically show a significant decrease in intensity with age, going from ∼10 A m^{-1} at the axis to ∼0–4 A m^{-1} after 10 Myr (Macdonald 1977; Bleil & Petersen 1983; Johnson & Pariso 1993). This reduction results from the low-temperature oxidation of titanomagnetite to titanomaghemite (Irving 1970; Marshall & Cox 1972). It may be represented by an exponential decay for which the characteristic time would be 5 Myr (Raymond & Labrecque 1987; Pockalny *et al.* 1995). We consider such an exponential decay, with maximum thermoremanent magnetization of extrusive basalts to be varying from 10 A m^{-1}at the axis to 2 A m^{-1} at 10 Myr. For intrusive basalts we adopt a maximum thermoremanent magnetization of 0.5 A m^{-1} (e.g. Dyment *et al.* 1997).

The basalt NRM may also present along-axis variations. Measurements on basalt samples dredged along four segments of the MAR at 26°S and 31–35°S (Weiland *et al.* 1996) and along the propagating spreading centre in the North Fiji Basin at 18–19°S (Horen & Fleutelot 1998) produce NRM values increasing by a factor of 2–3 from segment centre to ends. These observations are attributed to Fe-Ti enrichment of basalt at segment ends, as demonstrated by petrological measurements, and are a consequence of a higher fractionation degree, which in turn depends on the thermal structure. We simulate this effect by assuming the maximum remanent magnetization of basalt to be inversely proportional to the crustal thickness. To investigate the average effect of this variation, we adopt a factor of 2.5 between the maximum remanent magnetization at segment centre and ends.

Rock magnetic measurements on basalt samples (Wooldridge *et al.* 1992; Weiland *et al.* 1996) show systematically very high Koenigsberger ratios with an average value of 8, indicating that their induced magnetization is negligible.

Gabbro

The gabbro layer underlies the basalt layer and is assumed to be 4 km thick at segment centres. This value is suggested by seismic refraction experiments carried over several segments of the Mid-Atlantic Ridge between 34 and 36°S (Canales *et al.* 2000) and at 33°S (Tolstoy *et al.* 1993). These experiments indicate that the thickness of layer 3, interpreted as the gabbro layer, is 4 km at the segment centres.

Gabbro is often an olivine-rich rock, which acquires a chemical remanent magnetization and carries an induced magnetization. The remanent magnetization of gabbro increases with the rate of alteration: we consider that the maximum remanent magnetization varies linearly from 0 to 1 A m^{-1}, according to measurements on olivine gabbros dredged along the Mid-Atlantic Ridge (Kent *et al.* 1978) and drilled in the South–West Indian Ridge (Pariso & Johnson 1993).

The induced magnetization carried by gabbro is even lower: measurements show systematically very high Koenigsberger ratios with an average value of 8 (Kent *et al.* 1978; Pariso & Johnson 1993; Gee *et al.* 1997).

Peridotite

Peridotite also acquires a chemical remanent magnetization and carries an induced magnetization. Measurements on serpentinized peridotite samples from site ODP 670 (20–24°N) suggest that their amount of magnetite and magnetic properties (susceptibility and NRM) increase linearly with the rate of serpentinization (Bina & Henry 1990). The NRM is negligible for non-serpentinized peridotite and reaches 7 ± 3A m^{-1} for entirely serpentinized peridotites, as indicated by samples from ODP site 895 (located on the Hess Deep) and site 920 (located on the MAR axis). These samples are of the most representative serpentinized peridotites in the oceanic crust (Oufi *et al.* 2002). We have therefore adopted a 7 A m^{-1} NRM value for entirely serpentinized peridotite.

Measurements taken on serpentinized peridotite samples from various DSDP and ODP holes in the North Atlantic provide relatively low and highly variable Koenigsberger ratios Q (Bina & Henry 1990; Nazarova 1994; Oufi *et al.* 2002). Samples from the off-axis sites are strongly altered and show Q values generally lower than 1. Conversely, samples from ODP sites 670 and 920, located on the ridge axis, exhibit Q ratios varying from 0.5 to 2 with an average of 1 (Bina & Henry 1990; Oufi *et al.* 2002). On this basis we have adopted a value of 1 for the Koenigsberger ratio of serpentinized peridotite. The induced magnetization carried by these serpentinized peridotites is comparable to their remanent magnetization, and the total magnetization of serpentinized peridotites is about twice the remanent magnetization, if the latter is acquired in a normal geomagnetic field period, and quasi-null, if acquired in a reverse period.

The distribution of magnetization

The distribution of magnetization is calculated in vertical sections perpendicular to the axis. Along-axis variations of the petrological and thermal structures generate variations in the distribution of magnetization between those plans. We assume a simple petrological structure, with the thickness of each layer being proportional to the total thickness of the crust.

As already stated, deeper isotherms combined with the crustal attenuation at segment ends result in a thick serpentinized layer at the expense of the other layers. The contribution of magnetized peridotites may therefore be significant at segment ends.

Calculation of the magnetic anomaly amplitudes

The amplitudes of the magnetic anomalies are derived from the calculated magnetization distribution using the spectral method of Blakely (1996). Contributions of individual 200 m thick layers are added. The anomalies are calculated to the pole (i.e. assuming vertical geomagnetic field and magnetization vectors), on both flanks of the ridge, over a 10 Myr period.

4 RESULTS

Magnetized basalts

The contribution of thermoremanent and induced magnetization of basalt was considered first. If the rocks present a constant magnetization along the axis (i.e. no effect of fractionation is considered), the amplitude variation of the axial magnetic anomaly only reflects the variation of the magnetized layer thickness along the segment (Fig. 5, A1). Increasing the offset between adjacent segments results in higher amplitude variation in relation with the stronger crustal attenuation at segment ends (Fig. 5, A2 and A3). In all cases, amplitudes are higher at segment centres than at segment ends.

Whatever the offset, Curie isotherms of extrusive and intrusive basalt are clearly deeper than the base of their respective layer and do not affect the shape of the magnetized basaltic layer, which remains thicker at the segment centres than at the segment ends (Fig. 5, A1). A shallow Curie isotherm in the basalt layer (Grindlay *et al.* 1992) does not appear to be a viable explanation to account for the lower amplitude of the axial magnetic anomaly at segment centres.

Iron and titanium content variation

Again, only the basalt layer is considered, but now with along-axis variation of magnetization intensity to account for the Fe-Ti content variation resulting from magma fractionation. The magnetization of extrusive basalts increases from 10 to 25 A m^{-1} between segment centres and segment ends (0.5–1.25 A m^{-1} for intrusive basalts), an increase which corresponds approximately to a FeO content increase of 1 per cent (from 8.8 to 9.8 per cent) (Weiland *et al.* 1996).

If the variation of the magnetized layer thickness between segment centres and segment ends is small enough (that is to say if it varies by a factor smaller than 2.5), the effect of Fe-Ti content variation dominates, resulting in higher amplitudes of the axial magnetic anomaly at the segment ends. This is the case when segments are aligned or only slightly offset (Fig. 5, B1). However, the amplitude variation predicted by the simulation in the case of aligned segments remains smaller than the observed one (Fig. 5, B1). In the case of larger offsets, the effect of the thickness variation dominates and the axial magnetic anomaly amplitude is higher at segment centres, in contradiction with the observations (Fig. 5, B2 and B3). In short, the effect of Fe-Ti content variation is not sufficient to explain the observations, but may notably contribute to the magnetic signal in the case of small or null offset between adjacent segments.

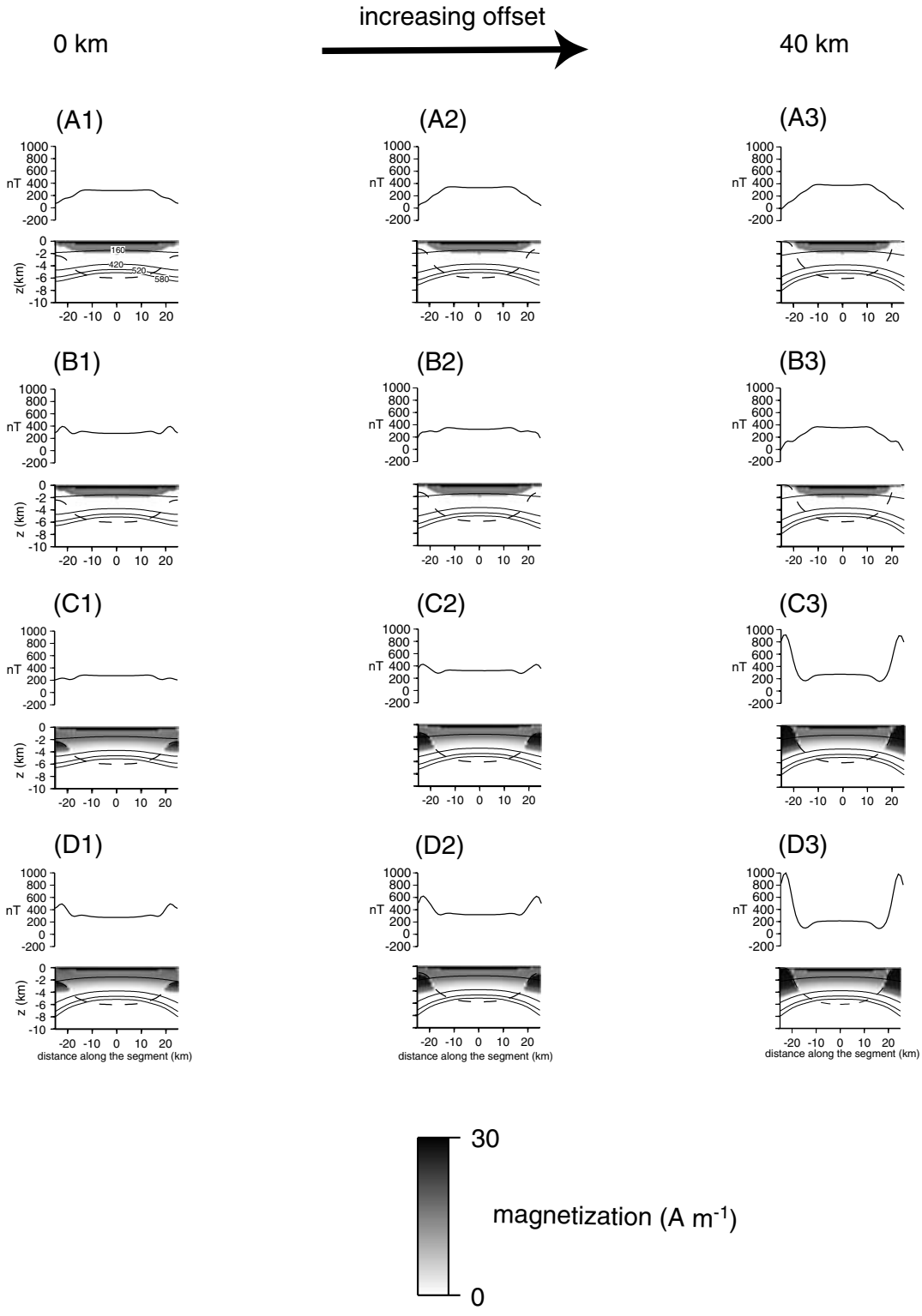

Figure 5. Axial magnetic anomaly computed from the different magnetization distribution models. The lower part of each plot represents the magnetization distribution in a vertical plane along the ridge axis. Shading shows the amount of magnetization. The isotherms of the blocking temperature ranges corresponding to each lithology (solid lines) and the Moho (dashed line) are also shown. The resulting axial magnetic anomaly along the axis is shown on the upper part of each plot. (A): only basalts bear a uniform magnetization. (B) only basalts bear a varying magnetization to reflect the effect of Fe-Ti content variation along the segment. (C) Same as (A), taking also into account the magnetization of serpentinized peridotites. (D) Same as (B), taking also into account the magnetization of serpentinized peridotites. In each case (A to D), the effect of the variable offsets with the neighbouring segment are considered (indexed 1 for no offset, 2 for 20 km, and 3 for 40 km).

Serpentinized peridotites and altered olivine gabbros

In a second step, chemical remanent and induced magnetizations of the serpentinized peridotite and altered olivine gabbro are now taken into account, in addition to the thermoremanent and induced magnetizations of basalt.

In the case of aligned or slightly offset (less than 20 km) segments, the crustal thickness at segment ends remains noticeable (∼2 km). The shallower peridotites are therefore emplaced at a depth of ∼2 km where the rate of serpentinization is lower than 50 per cent. This serpentinized peridotites therefore carry a low magnetization (maximum 1.2 A m^{-1}) and do not contribute significantly to the amplitude of the axial anomaly at segment ends. This contribution is not sufficient to compensate the attenuation of the strongly magnetized basaltic layer (Fig. 5, C1 and C2). Similarly, the olivine gabbro carries a weak magnetization (maximum 1 A m^{-1}), and brings a negligible contribution to the magnetic signal.

In the case of larger offsets between adjacent segments, the stronger crustal attenuation at segment ends may allow outcropping peridotite. Deeper isotherms result in a deeper serpentinization front, increasing the thickness of the serpentinized peridotite layer. For offsets larger than 20 km, the amount of serpentinized peridotites can produce axial magnetic anomalies with amplitudes twice to three times higher at segment ends than at segment centres (Fig. 5, C3).

Combination of two processes: variation of the Fe-Ti content and magnetization of the serpentinites

Previous results suggest that a combination of the two previous models may well explain the observations for the various offsets considered.

In the case of a large offset between segments (an offset larger than 20 km) the presence of serpentinized peridotites combined with higher Fe-Ti content and higher magnetization at segment ends produces an amplitude of the axial anomaly more than twice than that at the segment centres (Fig. 5, D3).

On the other hand, for a smaller or null offset between segments, we have shown that the effect of magnetized serpentinized peridotite roughly compensates for the attenuation of the magnetized basaltic layer at segment ends. Adding the variation of Fe-Ti content in basalt results in an axial magnetic anomaly amplitudes 1.5 times to twice as high at segment ends compared with segment centres (Fig. 5, D1 and D2).

Our computations show that varying the magnetic parameters within an acceptable range does not qualitatively modify the above results: the magnetic anomaly amplitude remains higher at segment ends than at segment centres, whatever the offset length. The variation of axial magnetic anomaly amplitude depends mainly on three factors: (1) the increase in basalt magnetization towards segment ends related to the Fe-Ti content variation (about 2–3); (2) the magnetization of serpentinized peridotites (maximum NRM between 4 and 10 A m^{-1}); and (3) the Koenigsberger ratio (from 0.5 to 2) of the peridotite. The influence of other magnetic parameters was shown to be secondary. For the lowest values of the basalt magnetization variation (=2) and of the magnetization of serpentinized peridotites (NRM =4 A m^{-1} for entirely serpentinized peridotite and $Q = 2$) the magnetic effect of serpentinized peridotites and Fe-Ti content variation at segment ends is a minimum, although it remains significantly higher than at segment centres (Fig. 6, A). Conversely, for the highest values of the parameters (respectively, 3, NRM =10 A m^{-1} and $Q = 0.5$) the axial magnetic anomaly amplitude at segment ends increases considerably (Fig. 6B) and becomes even exaggerated in the case of 40 km offset segments.

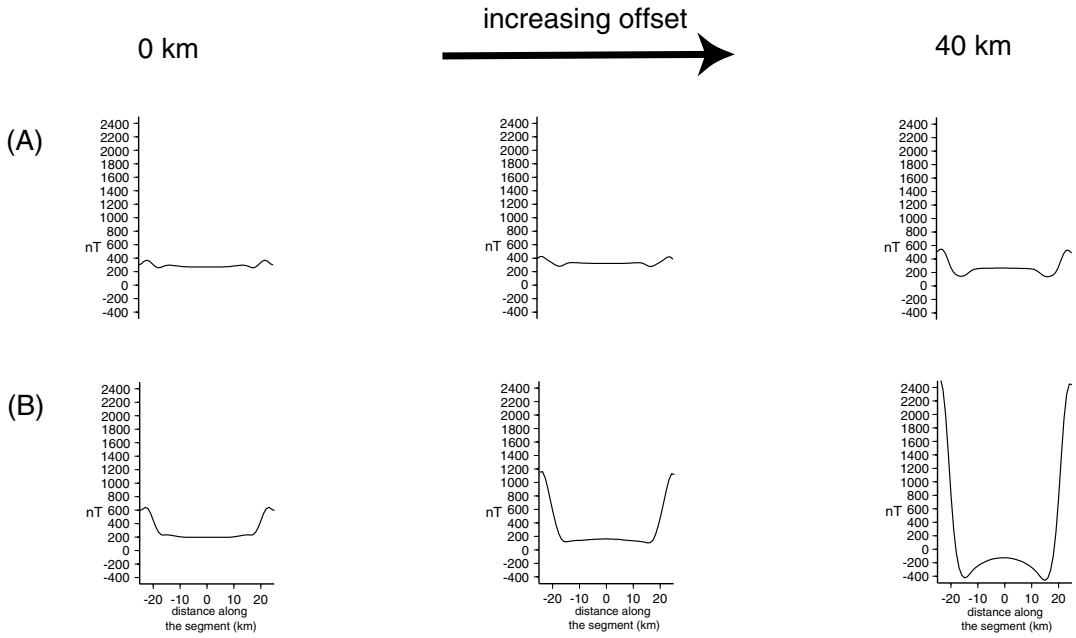

Figure 6. Effect of the three-dimensional parameters on modelled axial magnetic anomaly: increase factor in basalt magnetization between segment center and ends to the Fe-Ti content of the basalts., maximum magnetization and Koenigsberger ratio of the serpentinized peridotites. (A) Along-axis magnetic anomaly resulting from a minimum value of these parameters (increase factor = 2, serpentinized peridotites NRM = 4 A m^{-1} and $Q = 2$) for 0, 20 and 40 km offset segments (from left to right). (B) Along-axis magnetic anomaly resulting from a maximum value of these parameters (increase factot = 3, serpentinized peridotite NRM = 10 A m^{-1} and $Q = 4$).

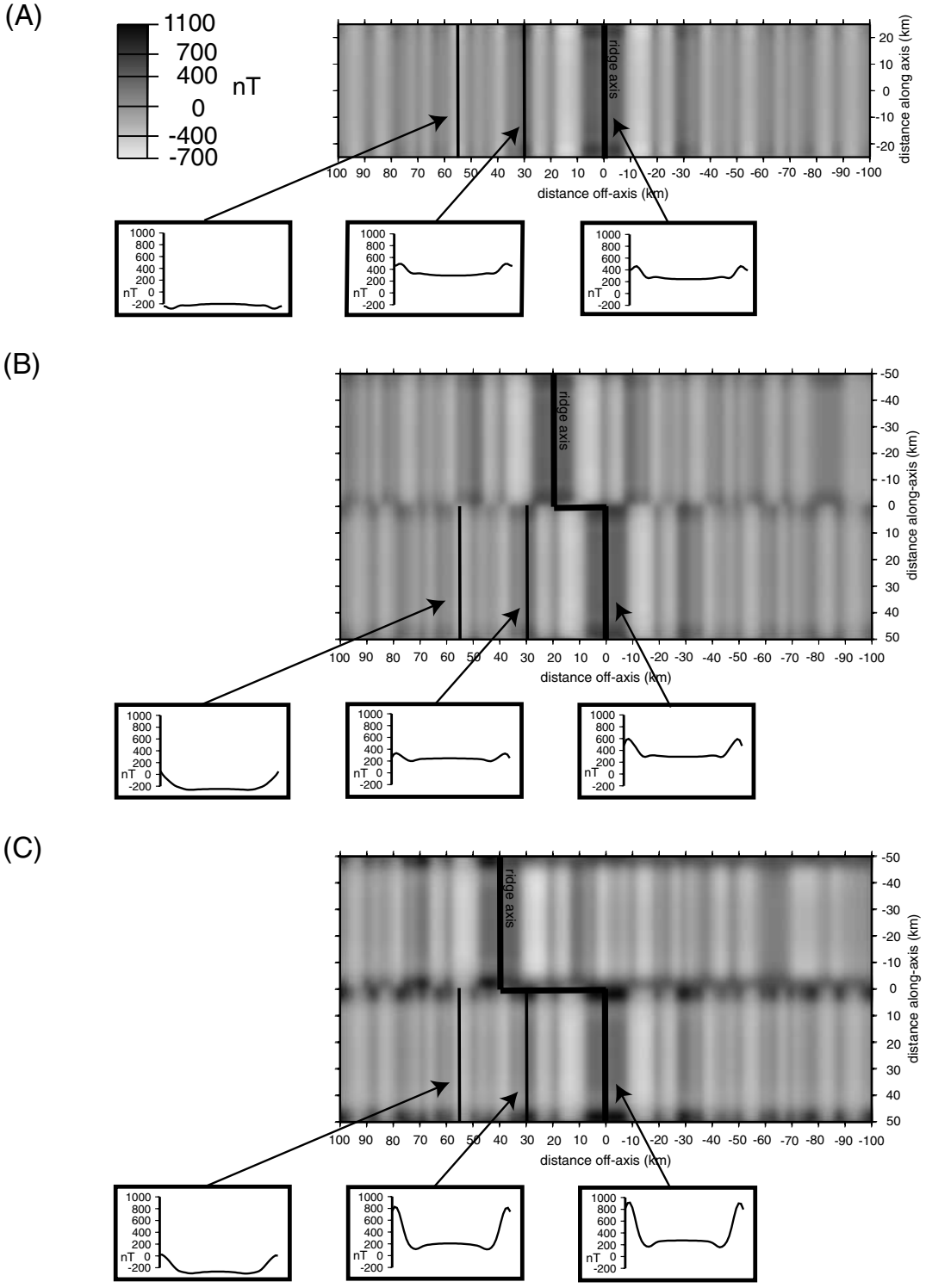

Figure 7. Modelled magnetic anomalies considering basalt (the Fe-Ti content variation is considered), gabbro and serpentinized peridotite magnetization (as shown along-axis on Fig. 5, D). (A) aligned segments; (B) 20 km offset segments and (C) 40 km offset segments. For each subset, *top*: modelled magnetic anomaly map; *bottom*: magnetic profiles along three isochrons. From left to right: sections along reversed chron 3r (5.5 Myr), normal chron 2A (3 Myr), and axis (0 Myr).

The combination of two processes, variation of the Fe-Ti content and magnetization of the serpentinites, therefore allows one to model a variation of the axial magnetic anomaly amplitude, twice as high as at segment ends than at segment centres. This result is in agreement with the observations: the axial magnetic anomaly observed along most segments of the Mid-Atlantic Ridge between 21°and 40°N (Ravilly *et al.* 1998) shows such a variation (Fig. 1).

Off-axis consequences

Our model also has implications on the off-axis magnetic structure. Along positive magnetic isochrones, the presence of serpentinized peridotites at segment ends and Fe-Ti content variation along the segment length result in variations of the magnetic anomaly amplitude similar to the axial one, although slightly attenuated due to decreasing basalt thermoremanent magnetization with age (Fig. 7, A–C). Conversely, along negative magnetic isochrones, serpentinized peridotites do not contribute significantly to the magnetic signal, as the contribution of their reversed remanent magnetization, negatively oriented, is cancelled by their normal-oriented induced magnetization. Consequently, the variation of the magnetic anomaly amplitude along negative magnetic isochrones is only controlled by the crustal thickness and Fe-Ti content variations. For small or null offset, as the stronger basalt magnetization at segment ends (due to the Fe-Ti content variation) dominates over the effect of the crustal thinning, the magnetic anomaly is slightly more negative at segment ends than at segment centres (Fig. 7, A). Conversely, in the case of larger offsets, the effect of the Fe-Ti content variation does not compensate that of the stronger crustal thinning at segment ends, and therefore, the magnetic anomaly amplitude is less negative at segment ends than at segment centres (Fig. 7, B and C).

Off-axis magnetic observations are scarce over the Mid-Atlantic Ridge. The variation in magnetic anomaly amplitudes, particularly in the negative ones, is not well constrained. It is therefore difficult to compare the outputs of our model with reliable data. Nevertheless, the off-axis magnetic study conducted in the SEADMA area, south of the Kane fracture zone (Pockalny *et al.* 1995) shows variations that seem to be in good agreement with our model: along negative isochrones, the magnetic anomaly amplitude becomes more positive close to first- and second-order discontinuities (corresponding to ∼20–40 km offset) and more negative close to third-order discontinuities (∼0–10 km offset). However, this last observation is contradicted by the data from the off-axis magnetic study conducted between 25°30′ and 27°10′N by Tivey & Tucholke (1998). Unlike the former study, these observations show that, along negative isochrones, the amplitude becomes more positive close to third-order discontinuities. More off-axis observations are therefore necessary to better constrain the variation of the magnetic anomaly amplitude along negative isochrones.

5 CONCLUSION

We have developed a thermal model of a slow-spreading ridge segment based on the hypothesis of a permanent hot zone beneath the segment centre. The shape and geometrical parameters of this zone have been adjusted to account for various geophysical observations, such as the along-axis variation of the gravity anomaly, the maximum depth of earthquakes and crustal structure. No parameters could be found that succeeded in modelling the observations for a hot zone with an elliptic base, simulating a very focused mantle upwelling under segment centres. Conversely, a good fit can be achieved with a hot zone that simulates a more sheet-like along-axis mantle upwelling. The best fit between model output and observations is reached for a hot zone with a constant section and a flat top, ∼10 km deep, along most of the segment length.

This best-fitting thermal intrusion has then been used to investigate the origin of the higher amplitude of axial magnetic anomaly at segment ends. Our modelling clearly shows that such an observation cannot be explained by shallower Curie isotherms resulting in a thinner basaltic magnetic layer at segment centres, as has often been proposed. The isotherms of titanomagnetite and magnetite are much deeper than the thickness of the extrusive and intrusive basaltic layers, respectively. Finally, the presence of serpentinized peridotites is sufficient to explain the observations for adjacent segments with large offsets, but this process needs to be coupled with Fe-Ti content variation in the basaltic layer to properly account for the amplitudes for segments with null or small offsets.

We therefore propose that both (1) the presence of serpentinized peridotites, due to shallower mantle material, colder temperatures and pervasive water circulation, at segments ends and (2) the Fe-Ti content variation related to varying degree of magma fractionation along the segment are the dominant processes explaining the observed variation of the axial magnetic anomaly amplitude.

ACKNOWLEDGMENTS

This work was funded by CNRS-INSU in the Programme 'Imagerie géophysique de la lithosphère et du manteau'. SG acknowledges a research fellowship from the French Ministry of Education and Research. We would like to thank our colleagues from the group DORSALES in Brest for fruitful discussions during the course of this work. We also thank Jafar Arkani-Hamed from McGill University (Montréal for discussions in the early stages of this project and two anonymous reviewers for many helpful suggestions that resulted in improvements to the text.

REFERENCES

Agrinier, P., Hekinian, R., Bideau, D. & Javoy, M., 1995. O and H stable isotope compositions of oceanic crust and upper mantle rocks exposed in the Hess Deep near the Galapagos Triple Junction, *Earth planet. Sci. Lett.,* **136,** 183–196.

Arkani-Hamed, J., 1988. Remanent magnetization of the oceanic upper mantle, *Geophys. Res. Lett.,* **15,** 48–51.

Arkani-Hamed, J., 1989. Thermoviscous remanent magnetization of oceanic lithosphere inferred from its thermal evolution, *J. geophys. Res.,* **94,** 17 421–17 436.

Barclay, A.H., Toomey, D.R., Purdy, G.M. & Solomon, S.C., 1993. FARA microearthquakes experiments III: Results from the Mid-Atlantic Ridge at 35°N, *AGU Fall meeting,* **74,** 601.

Becker, K. *et al.,* 1989. Ground-truth from the young oceanic crust at hole 504B, summary of results from DSDP/ODP Legs 69, 70, 83, 92 and 111, *Rev. Geophys.,* **27,** 79–102.

Bideau, D., Hébert, R., Hekinian, R. & Cannat, M., 1991. Metamorphism of deep-seated rocks from the Garrett ultrafast transform (East Pacific Rise near 13°25′S), *J. geophys. Res.,* **96,** 10 079–10 099.

Bina, M.M. & Henry, B., 1990. Magnetic properties, opaque mineralogy and magnetic anisotropies of serpentinized peridotites from ODP Hole 670A near the Mid-Atlantic Ridge, *Phys. Earth planet. Inter.,* **65,** 88–103.

Blakely, R.J., 1996. Fourier-domain modeling, in *Potential Theory in Gravity and Magnetic Applications*, pp. 258–311, Cambridge University Press, Cambridge.

Bleil, U. & Petersen, N., 1983. Variation in magnetization intensity and low temperature titanomagnetite oxidation of oceanic floor basalts, *Nature,* **301,** 384–388.

Calvert, A.J., 1995. Sesismic evidence for a magma chamber beneath the slow-spreading Mid-Atlantic Ridge, *Nature,* **377,** 410–414.

Canales, J.P., Detrick, R.S., Lin, J. & Collins, J.A., 2000. Crustal and upper mantle seismic structure beneath the rift moutains and across a nontransform offset at the Mid-Atlantic Ridge, *J. geophys. Res.,* **105,** 2699–2719.

Cannat, M., 1993. Emplacement of mantle rocks in the seafloor at mid-ocean ridges, *J. geophys. Res.,* **98,** 4163–4172.

Cannat, M. *et al.,* 1995. Thin crust, ultramafic rocks exposures, and rugged faulting pattern at the Mid-Atlantic Ridge (22°–24°N), *Geology,* **23,** 49–52.

Caruso, L.J. & Chernosky, J.V., 1979. The stability of lizardite, *Can. Min.,* **17,** 757–769.

Chen, W.P. & Molnar, P., 1983. Focal depths of intracontinental and intraplate earthquakes and their implications for the thermal and mechanical properties of the lithosphere, *J. geophys. Res.,* **88,** 4183–4214.

Christensen, N.I., 1966. Elasticity of ultrabasic rocks, *J. geophys. Res.,* **71,** 5921–5931.

Detrick, R.S., Needham, H.D. & Renard, V., 1995. Gravity anomalies and crustal thickness variations along the Mid-Atlantic Ridge between 33°N and 40°N, *J. geophys. Res.,* **100,** 3767–3787.

Dunlop, D.J. & Prévot, M., 1982. Magnetic properties and opaque mineralogy of drilled submarine intrusive rocks, *Geophys. J. R. astr. Soc.,* **69,** 763–802.

Dyment, J. & Arkani-Hamed, J., 1995. Spreading-rate-dependent magnetization of the oceanic lithosphere inferred from the anomalous skewness of marine magnetic anomalies, *Geophys. J. Int.,* **121,** 789–804.

Dyment, J., Arkani-Hamed, J. & Ghods, A., 1997. Contribution of serpentinized ultramafics to marine magnetic anomalies at slow and intermediate spreading centres: insights from the shape of the anomalies, *Geophys. J. Int.,* **129,** 691–701.

Fisher, A.T.K., Becker, T.N., Narasimhan, M.G. & Mottl, M.J., 1990. Passive off-axis convection on the southern flank of the Costa Rica Rift, *J. geophys. Res.,* **95,** 9343–9370.

Fisher, A.T., Becker, K. & Narasimhan, T.N., 1994. Off-axis hydrothermal circulation: parametric tests of a refined model of processes at Deep Sea Drilling Project/Ocean Drilling Program site 504, *J. geophys. Res.,* **99,** 3097–3121.

Francis, T.J.G., 1981. Serpentinization faults and their role in the tectonics of slow spreading ridges, *J. geophys. Res.,* **86,** 11 616–11 622.

Gee, J.S., Lawrence, R.M. & Hurst, S.D., 1997. Remanence characteristics of gabbros from the MARK area: implications for crustal magnetization, *Proc. Ocean Drill. Program Sci. Results,* **153,** 429–436.

Gente, P. *et al.,* 1995. Characteristics and evolution of the segmentation of the Mid-Atlantic Ridge between 20°N and 24°N during the last 10 million years, *Earth planet. Sci. Lett.,* **129,** 55–71.

Grindlay, N.R., Fox, P.J. & Vogt, P.R., 1992. Morphology and tectonics of the Mid-Atlantic Ridge (25°S–27°30′S) from SeaBeam and magnetic data, *J. geophys. Res.,* **97,** 6983–7010.

Hooft, E.E.E., Detrick, R.S., Toomey, D.R., Collins, J.A. & Lin, J., 2000. Crustal thickness and structure along three contrasting spreading segments of the Mid-Atlantic Ridge, 33.5°–35°N, *J. geophys. Res.,* **105,** 8205–8226.

Horen, H. & Fleutelot, C., 1998. Highly magnetized and differentiated basalts at the 18–19°S propagating spreading centre in the North Fidji Basin, *Mar. geophys. Res.,* **20,** 129–137.

Horen, H., Zamora, M. & Dubuisson, G., 1996. Seismic waves velocities and anisotropy in serpentinized peridotites from Xigaze ophiolite: abundance of serpentinite in slow spreading ridge, *Geophys. Res. Lett.,* **23,** 9–12.

Irving, E., 1970. The Mid-Atlantic Ridge at 45°N, XIV, oxidation and magnetic properties of basalts: review and discussion, *Can. J. Earth Sci.,* **7,** 1528–1538.

Johnson, H.P. & Pariso, J.E., 1993. Variations in oceanic crustal magnetization; systematic changes in the last 160 million years, *J. geophys. Res.,* **98,** 435–445.

Juteau, T., Cannat, M. & Lagabrielle, Y., 1990. Serpentinized peridotites in the upper oceanic crust away from transform zones: a comparison of the results of previous DSDP and ODP legs, *Proc. Ocean Drill. Program Sci. Results,* **106–109,** 303–308.

Kent, D.V., Honnores, B.M., Opdyke, N.D. & Fox, P.J., 1978. Magnetic properties of dredged oceanic gabbros and the source of marine magnetic anomalies, *Geophys. J. R. astr. Soc.,* **55,** 513–537.

Kong, L.S.L., Solomon, S.C. & Purdy, G.M., 1992. Microearthquake characteristics of a Mid-Ocean Ridge along-axis high, *J. geophys. Res.,* **97,** 1659–1685.

Kuo, B.Y. & Forsyth, D.W., 1988. Gravity Anomaly of the Ridge Transform System in the South Atlantic between 31 and 34.5°S: upwelling centers and variation in crustal thickness, *Mar. geophys. Res.,* **10,** 205–232.

Le Douaran, S. & Francheteau, J., 1981. Axial depth anomalies from 10 to 50° North along the Mid-Atlantic Ridge: correlation with other mantle properties, *Earth planet Sci. Lett.,* **54,** 29–47.

Lin, J. & Phipps Morgan, J., 1992. The spreading rate dependence of three-dimensional mid-ocean ridge gravity structure, *Geophys. Res. Lett.,* **19,** 13–16.

Lin, J., Purdy, G.M., Schouten, H., Sempéré, J.C. & Zervas, C., 1990. Evidence from gravity data for focused magmatic accretion along the Mid-Atlantic Ridge, *Nature,* **344,** 627–632.

Macdonald, K.C., 1977. Near-bottom magnetic anomalies, asymmetric spreading, oblique spreading, and tectonics of the Mid-Atlantic Ridge near lat. 37°N, *Geol. Soc. Am. Bull.,* **88,** 541–555.

Macdonald, A.H. & Fyfe, W.S., 1984. Rate of serpentinization in seafloor environments, *Tectonophysics,* **116,** 123–135.

Macdonald, K.C., Sempéré, J.C. & Fox, P.J., 1984. East Pacific Rise from Siquieros to Orozco Fractures Zones: along-strike continuity of axial neovolcanic zone and structure and evolution of overlapping spreading centers, *J. geophys. Res.,* **3,** 211–215.

Macdonald, K.C., Sempéré, J.C. & Fox, P.J., 1986. Reply: the debate concerning overlapping spreading centers and mid-ocean ridge processes, *J. geophys. Res.,* **91,** 10 501–10 511.

Magde, S.G. & Sparks, D.W., 1997. Three-dimensional mantle upwelling, melt generation, and melt migration beneath segment slow-spreading ridges, *J. geophys. Res.,* **102,** 20 571–20 583.

Magde, S.G., Sparks, D.W. & Detrick, R.D., 1997. The relation between buoyant mantle flow, melt migration and gravity bull's eyes at the Mid-Atlantic Ridge between 33°N and 35°N, *Earth planet. Sci. Lett.,* **148,** 59–67.

Marshall, M. & Cox, A., 1972. Magnetic changes in pillow basalt due to sea-floor weathering, *J. geophys. Res.,* **77,** 6459–6469.

McKenzie, D., 1984. The generation and compaction of partially molten rock, *J. Petro.,* **25,** 713–765.

Miller, D.J. & Christensen, N.I., 1997. Seismic velocities of lower crustal and upper mantle rocks from the slow spreading Mid-Atlantic Ridge, south of the Kane transform zone (MARK), *Proc. Ocean Drill. Program Sci. Results,* **153,** 437–454.

Nazarova, K.A., 1994. Serpentinized peridotites as a possible source for oceanic magnetic anomalies, *Mar. geophys. Res.,* **16,** 455–462.

Nicolas, A., 1989. *Structure of Ophiolites and Dynamics of Oceanic Lithosphere,* p. 367, Kluwer, Dordrecht.

Niu, Y. & Batiza, R., 1994. Magmatic processes at a slow-spreading ridge segment: 26°S Mid-Atlantic Ridge, *J. geophys. Res.,* **99,** 19 719–19 740.

Noye, J., 1984. Finite difference techniques for partial differential equations, in *Computational Techniques for Differential Equations*, pp. 95–353, ed. Noyes, J., North-Holland Mathematic Studies, North-Holland, Amsterdam.

Oufi, O., Cannat, M. & Horen, H., 2002. Magnetic properties of variably serpentinized abyssal peridotites, *J. geophys. Res.,* **107,** 1–20.

Pariso, J.E. & Johnson, H.P., 1993. Do lower crustal rocks record reversals of the Earth's magnetic field? Magnetic petrology of oceanic gabbros from Ocean Drilling Program Hole 735B, *J. geophys. Res.,* **98,** 16 013–16 032.

Pariso, J.E., Rommevaux, C. & Sempéré, J.C., 1996. Three-dimensional inversion of marine magnetic anomalies: implications for crustal accretion along the Mid-Atlantic Ridge (28°–31°30′N), *Mar. geophys. Res.,* **18,** 85–101.

Pockalny, R.A., Detrick, R.S. & Fox, P.J., 1988. Morphology and tectonics of the Kane transform from Sea Beam bathymetry data, *J. geophys. Res.,* **93,** 3179–3193.

Pockalny, R.A., Smith, A. & Gente, P., 1995. Spatial and temporal variability of crustal magnetization of a slowly spreading ridge: Mid-Atlantic Ridge (20°–24°N), *Mar. geophys. Res.,* **17,** 301–320.

Pozzi, J.P. & Dubuisson, G., 1992. High temperature viscous magnetization of oceanic deep crustal and mantle rocks as a partial source for Magsat magnetic anomalies, *Geophys. Res. Lett.,* **19,** 21–24.

Ravilly, M., Dyment, J., Gente, P. & Thibaud, R., 1998. Axial magnetic anomaly amplitude along the Mid-Atlantic Ridge between 20°N and 40°N, *J. geophys. Res.,* **103,** 24 201–24 221.

Raymond, C.A. & Labrecque, J.L., 1987. Magnetization of the oceanic crust: thermoremanent magnetization or chemical remanent magnetization?, *J. geophys. Res.,* **92,** 8077–8088.

Rona, P.A., 1978. Magnetic signatures of hydrothermal alteration and volcanogenic mineral deposits in oceanic crust, *J. volcanol. geotherm. Res.,* **3,** 219–225.

Scott, D.R. & Stevenson, D.J., 1989. A self-consistent model of melting, magma migration and buoyancy-driven circulation beneath mid-ocean ridges, *J. geophys. Res.,* **94,** 2973–2988.

Sempéré, J.C., Purdy, G.M. & Schouten, H., 1990. Segmentation of the Mid-Atlantic Ridge between 24°N and 30°40′N, *Nature,* **344,** 427–431.

Sempéré, J.C., Lin, J., Brown, H.S., Schouten, H. & Purdy, G.M., 1993. Segmentation and morphotectonic variations along a slow-spreading center: the Mid-Atlantic Ridge (24°00′N–30°40′N), *Mar. geophys. Res.,* **15,** 153–200.

Sinton, J.M. & Detrick, R.S., 1992. Mid-Ocean Ridge magma chambers, *J. geophys. Res.,* **97,** 197–216.

Thibaud, R., Gente, P. & Maia, M., 1998. A systematic analysis of the Mid-Atlantic Ridge morphology and gravity between 15°N and 40°N: constraints of the thermal structure, *J. geophys. Res.,* **103,** 24 223–24 243.

Tisseau, C. & Tonnerre, T., 1995. Non steady-state thermal model of spreading ridges: implication for melt generation and mantle outcrops, in *Mantle and Lower Crust Exposed in Ridges and Ophiolites,* pp. 181–214, eds Vissers, R.L.M. & Nicolas, A., Kluwer, Dordrecht.

Tivey, M.A. & Tucholke, B.E., 1998. Magnetization of 0–29 Ma ocean crust on the Mid-Atlantic Ridge, 25°30′ to 27°10′N, *J. geophys. Res.,* **103,** 17 807–17 826.

Tolstoy, M., Harding, A.J. & Orcutt, J.A., 1993. Crustal thickness on the Mid-Atlantic Ridge: bull's eye gravity anomalies and focused accretion, *Science,* **262,** 726–729.

Toomey, D.R., Solomon, S.C., Purdy, G.M. & Murray, M.H., 1985. Microearthquakes beneath the median valley of the Mid-Atlantic Ridge near 23°N: hypocenters and focal mechanisms, *J. geophys. Res.,* **90,** 5443–5458.

Toomey, D.R., Solomon, S.C. & Purdy, G.M., 1988. Microearthquakes beneath the median valley of the Mid-Atlantic Ridge near 23°N: tomography and tectonics, *J. geophys. Res.,* **93,** 9093–9112.

Toomey, D.R., Purdy, G.M., Barclay, A.H., Wolfe, C.J. & Solomon, S.C., 1993. FARA microearthquakes experiments IV: implications of Mid-Atlantic Ridge seismicity for models of young oceanic lithosphere, *AGU Fall meeting,* **74,** 601.

Trutin, F., 1995. Modélisation 3D de l'évolution dans le temps de la structure thermique de l'axe d'une dorsale océanique, *Rapport de DEA,* Université de Bretagne Occidentale, Brest.

Tucholke, B.E. & Schouten, H., 1988. Kane Fracture zone, *Mar. geophys. Res.,* **10,** 1–39.

Weiland, C.M., Macdonald, K.C. & Grindlay, N.R., 1996. Ridge segmentation and the magnetic structure of the southern Mid-Atlantic Ridge 26°S and 31°–35°S: implications for magmatic processes at slow spreading centers, *J. geophys. Res.,* **101,** 8055–8073.

Whitehead, J.A., Dick, H.J.B. & Schouten, H., 1984. A mechanism for magmatic accretion under spreading centers, *Nature,* **312,** 146–147.

Wolfe, C.J., Purdy, G.M., Toomey, D.R. & Solomon, S.C., 1995. Microearthquake characteristics and crustal velocity structure at 29°N on the Mid-Atlantic Ridge: the architecture of a slow spreading ridge, *J. geophys. Res.,* **100,** 24 449–24 472.

Wooldridge, A.L., Harrison, C.G.A., Tivey, M.A. & Rona, P.A., 1992. Magnetic modeling near selected areas of hydrothermal activity on the Mid-Atlantic Ridge and Gorda Ridge, *J. geophys. Res.,* **97,** 10 911–10 926.

Yanenko, N.N., 1968. *Méthode à pas fractionnaire Résolution des Problèmes Polydimensionnels de Physique Mathématique*, p. 205, Armand Colin, Paris.